Available online at www.sciencedirect.com

SciVerse ScienceDirect

Ceramics International 39 (2013) 6399–6405

CERAMICS INTERNATIONAL

www.elsevier.com/locate/ceramint

Structural, vibrational, optical, magnetic and dielectric properties of $Bi_{1-x}Ba_xFeO_3$ nanoparticles

Sunil Chauhan, Manisha Arora, P.C. Sati, Sandeep Chhoker, S.C. Katyal, Manoj Kumar*

Department of Physics & Material Science & Engineering, Jaypee Institute of Information Technology, Noida 201307, India

Received 29 December 2012; received in revised form 19 January 2013; accepted 21 January 2013
Available online 31 January 2013

Abstract

$Bi_{1-x}Ba_xFeO_3$ ($x=0.05$, 0.10 and 0.15) nanoparticles were synthesized by the sol–gel method. X-ray diffraction and Raman spectroscopy results showed the presence of distorted rhombohedral structure of $Bi_{1-x}Ba_xFeO_3$ nanoparticles. Rietveld refinement and Williamson–Hall plot of the x-ray diffraction patterns showed the increase in lattice parameters, unit cell volume and the particle size. Infrared spectroscopy and Raman analysis revealed the shifting of phonon modes towards the higher wavenumber side with increasing Ba concentration. These samples exhibited the optical band gap in the visible region (2.47–2.02 eV) indicating their ability to absorb visible light. Magnetic measurement showed room temperature ferromagnetic behavior, which may be attributed to the antiferromagnetic core and the ferromagnetic surface of the nanoparticles, together with the structural distortion caused by Ba substitution. The magnetoelectric coupling was evidenced by the observation of the dielectric anomaly in the dielectric constant and the dielectric loss near antiferromagnetic Neel temperature in all the samples.

Keywords: C. Optical properties; C. Magnetic properties; Multiferroics; Nanoparticles; Raman spectroscopy

1. Introduction

Multiferroic materials which show ferroelectricity (antiferroelectricity) and ferromagnetism (antiferromagnetism) simultaneously in the same phase have attracted much attention for their potential applications in the emerging field of spintronics, data storage media, sensors and multistate memories and for their unique physical characteristics [1–5]. However, naturally occurring multiferroic materials are rare as the ferroelectricity in ABO_3 type of perovskite needs d^0ness electronic configuration of transition metal ions, whereas magnetism needs partially filled d orbitals of transition metal ions. These two requirements for the exhibition of ferroelectricity and ferromagnetism within a single phase are mutually exclusive to each other [2]. $BiFeO_3$ (BFO) belongs to ABO_3 type of compounds that shows ferroelectricity and antiferromagnetism in the single phase at room temperature and has rhombohedrally distorted perovskite structure with space group R3c. From the practical application point of view it is the most promising material due to its high ferroelectric Curie-temperature ($T_C \sim 1103$ K) and antiferromagnetic Neel temperature ($T_N \sim 643$ K) [6]. In BFO, ferroelectricity arises due to stereochemically active $6s^2$ lone pair electrons of the Bi^{3+} ions, while magnetic behavior appears due to the Fe^{3+} ions. However, no macroscopic magnetization is observed in BFO due to its spiral spin structure along the $[110]_h$ axis at room temperature. In this spiral spin structure, the antiferromagnetic axis rotate through the crystal with an incommensurate long wavelength period of 62 nm, which cancels the macroscopic magnetization (weak ferromagnetism).

It is widely expected that the strategies based on nanotechnology and divalent cation, transition metal ion and rare earth metal ion substitution will have a great impact on their magnetic, electric, optical and magnetoelectric properties. Interestingly, the magnetic properties enhancement of BFO ceramics doped with lone pair active divalent ions is comparable to the rare earth and transition metal (magnetic) ions doped BFO ceramics [7–10]. In addition to the potential magnetoelectric property based

*Corresponding author. Tel.: +91 120 2594386; fax: +91 120 2400986.
E-mail address: manoj.chauhan@jiit.ac.in (M. Kumar).

0272-8842/$ - see front matter © 2013 Elsevier Ltd and Techna Group S.r.l. All rights reserved.
http://dx.doi.org/10.1016/j.ceramint.2013.01.066

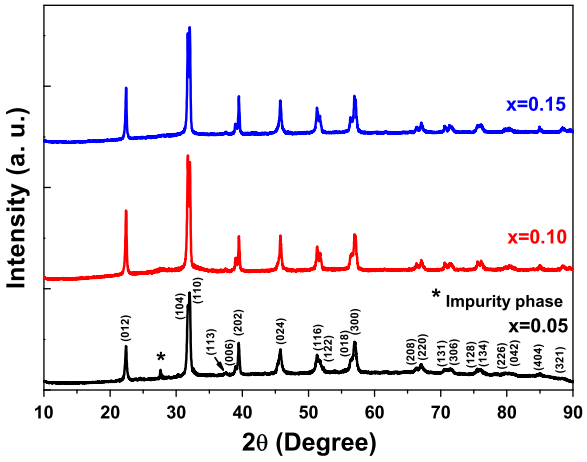

Fig. 1. XRD patterns of $Bi_{1-x}Ba_xFeO_3$ samples calcined at 600 °C.

applications, BFO has interesting optical properties and may find applications as photocatalytic material, solar cell material and ferroelectric ultrafast optoelectronic devices [11,12]. There are few reports available on Ba doped BFO ceramics showing the promising multiferroic properties [13,14]. However, no detail study is available on structural analysis by Raman spectroscopy and optical properties of Ba doped BFO nanoparticles. In the present communication, we report the structural, optical, magnetic and dielectric properties $Bi_{1-x}Ba_xFeO_3$ nanoparticles.

2. Experimental

$Bi_{1-x}Ba_xFeO_3$ nanoparticles with $x=0.05$, 0.10 and 0.15 were prepared by the sol–gel method. All the chemical reagents used as starting materials were analytic grade reagents and do not require additional treatment. In a typical process, calculated amounts of bismuth nitrate ($Bi(NO_3)_3\cdot 5H_2O$), ferric nitrate ($Fe(NO_3)_3\cdot 9H_2O$) and barium nitrate ($Ba(NO_3)_2\cdot 6H_2O$) were dissolved in deionized water. As $Bi(NO_3)_3\cdot 5H_2O$ undergoes decomposition into bismuth oxychloride in water, it was first taken in 50 ml deionized water and kept on stirring. During stirring dilute nitric acid was added drop by drop until a clear and transparent solution was obtained which confirmed the complete dissolution of $Bi(NO_3)_3\cdot 5H_2O$ then ferric nitrate and barium nitrate were added. The stoichiometric amount of tartaric acid ($C_6H_6O_7$) was further added for the complete combustion of the nitrates [15,16]. The yellow transparent solution was stirred vigorously for 12 h over a hot plate kept at 60 °C. Further the transparent solution was dried for two days in an oven maintained at 120 °C to get the fluffy gel. Finally, the fluffy gel was calcined at 600 °C for two and half hrs in an air ambience resulting in the phase formation of $Bi_{1-x}Ba_xFeO_3$ nanoparticles.

The powder X-ray diffraction (XRD) was employed to study the crystal structure of the samples using Shimadzu XRD-6000 diffractometer with CuKα (λ=1.5406 Å) radiation. Field emission scanning electron microscopy (FESEM) was used to determine grain size and uniformity of the sample matrix. The UV–Visible (UV–vis) spectra were recorded over a range of 350–1100 nm wavelength using Perkin Elmer Lambda-750 UV/Vis/NIR spectrometer. The sample powders were uniformly dispersed in ethanol solution followed by ultrasonication for 20–30 min before recording UV–vis spectra. The vibrational properties were characterized by Fourier Transformed Infrared (FTIR) spectroscopy performed on a Varian 7000 FTIR spectrometer with the spectral resolution of 1 cm^{-1}. The FTIR measurements of all the samples were done using the KBr pellet method in the wavenumber range 400–4000 cm^{-1} at room temperature. Raman spectroscopy was carried out in the backscattering configuration (LabRAM HR) with charge coupled device detector and 514.5 nm Laser beam. The Laser power was kept below 2 mW in order to avoid any sample heating. The room temperature magnetization hysteresis (M–H) loops of prepared nanoparticles were measured using a Vibrating Sample Magnetometer (VSM, Princeton Applied Model 155). The dielectric measurements were done on silver coated pellets using HIOKI 3522-50 LCR Hi-Tester.

3. Results and discussion

Fig. 1 illustrates the XRD patterns of $Bi_{1-x}Ba_xFeO_3$ nanoparticles with $x=0.05$, 0.10 and 0.15. All the XRD patterns expectedly show the typical peaks of rhombohedral structure (JCPDS card number 71-2494) indicating the presence of highly crystalline BFO nanoparticles. However, a very small broad peak at 2θ value of 27° is observed which is assigned to $Bi_{25}FeO_{40}$ phase (JCPDS card number 46-0416) in $x=0.05$ sample. However, this impurity phase suppressed with increasing Ba concentration and phase pure $Bi_{1-x}Ba_xFeO_3$ nanoparticles were obtained for $x=0.10$ and 0.15. The effect of the doping on the crystal structure of $Bi_{1-x}Ba_xFeO_3$ nanoparticles was analyzed by using Rietveld refinement tool 'FullProf' [17]. The Rietveld refinement was carried out by considering *R3c* space group with ionic positions of Bi/Ba at

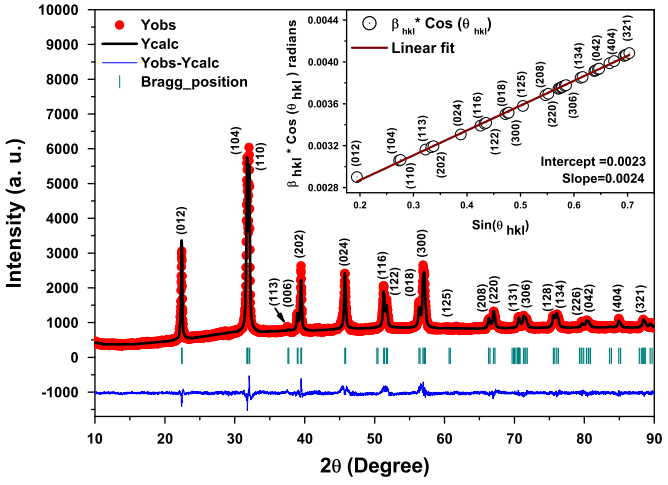

Fig. 2. Rietveld refined pattern of $Bi_{0.85}Ba_{0.15}FeO_3$ nanoparticles. Inset shows Williamson–Hall plot of $Bi_{0.85}Ba_{0.15}FeO_3$ nanoparticles.

6a, Fe at 6a and O at 18b [18]. The Bragg peaks were modeled with Thompson–Cox–Hastings pseudo-Voigt function and the background was estimated by linear interpolation between selected background points. Fig. 2 features the observed, calculated and difference XRD profiles for $x=0.15$ sample after final cycle of refinement. It was noticed that the observed and calculated profiles correspond each other. The value of χ^2 was found to be 2.12 which is suitable for estimation. The profile fitting procedure was adapted to minimize the χ^2 function [19]. The refined structural parameters were found to be $a=b=5.5795$ Å, $c=13.8540$ Å, and $V=373.265$ Å^3: $a=b=5.5806$ Å, $c=13.8631$ Å, and $V=373.908$ Å^3: and $a=b=5.5871$ Å, $c=13.8653$ Å, and $V=374.120$ Å^3 for $x=0.05$, 0.10 and 0.15 samples respectively. These structural parameters confirmed that the Bi^{3+} ions were substituted by the Ba^{2+} ions in BFO lattice. The unit cell volume increases with increasing x in $Bi_{1-x}Ba_xFeO_3$ samples, since the ionic radius of Ba^{2+} (1.49 Å) is greater than that of Bi^{3+} (1.17 Å). Also the Fe–O–Fe bond angles increase with increasing x, indicating the distortion in rhombohedral structure caused by the Ba^{2+} substitution.

The particle size and lattice strain of $Bi_{1-x}Ba_xFeO_3$ samples were calculated from the broadening of the XRD peaks using Williamson–Hall approach [20]. The observed line breadth is simply the sum of two contributions given by Williamson–Hall equation:

$$\beta_{hkl} = (K \times \lambda/D \times \cos(\theta_{hkl})) + \eta \times \tan(\theta_{hkl}) \quad (1)$$

The first term, $[K \times \lambda/(D \times \cos(\theta_{hkl}))]$, on the right hand side in Eq. (1) represents the size broadening and the second term, $[\eta \times \tan(\theta_{hkl})]$, represents microstrain broadening. After plotting the graph between $\beta_{hkl} \times \cos(\theta_{hkl})$ and $\sin(\theta_{hkl})$, microstrain was calculated from the slope of the line and the particle size D was calculated from the intersection ($\lambda/D = Intersection$) with the vertical axis. Inset of Fig. 2 shows the Williamson–Hall plot for $x=0.15$ sample. From these calculations, it was found that average particle size increases from 35 to 67 nm with increasing Ba content from $x=0.05$ to $x=0.15$ in BFO samples. Fig. 3 shows the FESEM images of $Bi_{1-x}Ba_xFeO_3$ nanoparticles sintered at 600 °C. The morphology is dense and uniform and the grain size varies in the range 50–200 nm. The grain size of the samples increases with increasing Ba content in BFO which is in agreement with particle size calculated from XRD results.

Infrared spectroscopy (IR) is an effective tool to study the structural properties of oxide materials. The XRD results showed distorted rhombohedral crystal structure with space group $R3c$ for $Bi_{1-x}Ba_xFeO_3$ samples. The group theory predicts that BFO in R3c space group should display optical phonon modes given by $\Gamma_{opt}(R3c) = 4A_1^{IR,R} \oplus 9E^{IR,R} + 5A_2$ [21]. The A_1 and E modes are both IR and Raman active whereas the A_2 modes are IR and Raman inactive. Further, the phonon modes A_1 and E are transverse optical (TO) vibrational modes. The room temperature Raman spectra of $Bi_{1-x}Ba_xFeO_3$ nanoparticles are shown in Fig. 4. *Density functional theory calculations were performed by Hermet et al. [22] within the local spin density approximation (LSDA) as implemented in the ABINIT package*. The assignment of the observed vibration modes are based on calculations carried out by Hermet et al. and experimentally reported Raman data by Porporati et al. and IR data by Chen et al. [21–23]. As summarized in Table 1, we have observed eleven TO vibrational modes (three A_1(TO)+eight E(TO)) in the Raman spectra of $Bi_{1-x}Ba_xFeO_3$ samples. Since the Raman spectra are sensitive to atomic displacements, the shift in the Raman modes with increasing Ba content in BFO samples can provide valuable information about ionic substitution, lattice distortion and electric polarization. The lower wavenumber vibration modes below 170 cm^{-1} give the information about Bi atoms and the oxygen motion strongly dominates in the modes above 267 cm^{-1} [22]. The Fe atoms are mainly involved in the

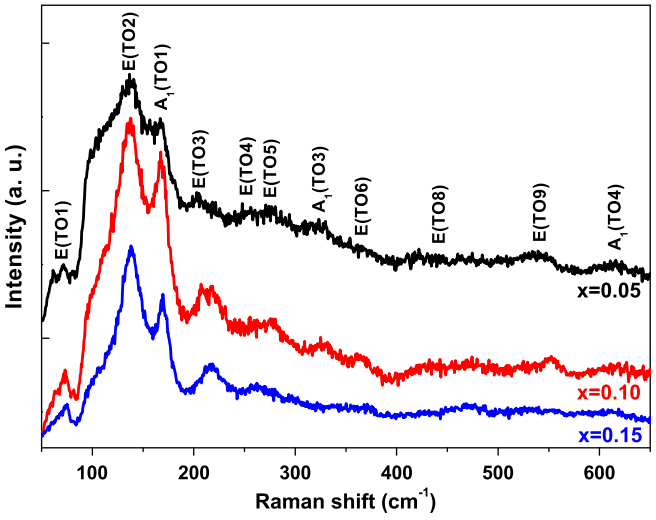

Fig. 4. Raman spectra of $Bi_{1-x}Ba_xFeO_3$ nanoparticles at room temperature.

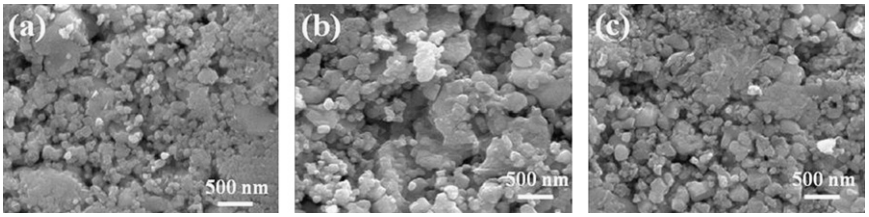

Fig. 3. FESEM images of $Bi_{1-x}Ba_xFeO_3$ nanoparticles, (a) $x=0.05$, (b) $x=0.10$ and $x=0.15$.

modes between 152 and 261 cm^{-1} and also contribute to some higher wavenumber modes. The E(TO1) and E(TO2) modes, which are governed by Bi–O covalent bond, shifted toward higher wavenumber with increasing Ba concentration, indicating that the dopants entered into the Bi site of BFO lattice. The vibrational frequency of Bi/Ba–O bond of $Bi_{1-x}Ba_xFeO_3$ nanoparticles can be determined from the band position of the E(TO1) and E(TO2) modes using, $v = 1/2\pi c\sqrt{(K/\mu)}$, where v is the wavenumber, c the velocity of light, K average force constant of the Bi/Ba–O bond and the effective mass μ is given by $\mu = M_O \times [xM_{Bi} + (1-x)M_{Ba}]/M_O + [xM_{Bi} + (1-x)M_{Ba}]$, where M_O, M_{Bi} and M_{Ba} are the atomic weights of O, Bi and Ba, respectively [24]. From the above mentioned equations, the effective mass of Bi/Ba–O bond decreases with increasing Ba substitution because of the lower atomic weight of the Ba atom than that of the Bi atom. Hereby mentioned changes in local structure parameters can only be possible with the incorporation of the Ba ions at Bi site into BFO lattice.

The room temperature FTIR spectra of $Bi_{1-x}Ba_xFeO_3$ nanoparticles are shown in Fig. 5. Normally the absorption modes within 1000 cm^{-1} range are attributed to the bonds between inorganic elements. Three vibration (TO) modes at 445, 530 and 580 cm^{-1} defined as E(TO8), E(TO9) and A_1(TO4) within 400–650 cm^{-1} range are the characteristics modes of BFO. These modes are consistence with the previously reported data [21]. The broad nature of the observed vibration bands is due to the occurrence of absorption peaks of both Fe–O and Bi/Ba–O bonds at nearly the same wavenumber (inset of Fig. 5). The broad absorption bands at 445 cm^{-1} [E(TO8)] and 575 cm^{-1} [A_1(TO4)] are assigned to the bending vibration of the O–Fe–O bond and stretching vibration of the Fe–O bond, respectively, present in the FeO_6 octahedral unit. Also, the absorbance bands at 450 cm^{-1} and 530 cm^{-1} [E(TO9)] are attributed to the vibration modes of Bi/Ba–O present in the Bi/BaO_6 octahedral unit (Fig. 5 inset) [21,25,26]. The broad peak around 3450 cm^{-1} represents the stretching vibrations of the O-H group, whereas the two absorption peaks around 2337 and 2362 cm^{-1} correspond to CO_2 modes. These CO_2 modes may arise due to some trapped CO_2 in the air ambience during the FTIR characterization. The presence of very small carbonate phase is verified by the observation of the bands around the wavenumber 856 and 1444 cm^{-1} [27] which could not be detected in the XRD patterns. The various higher wavenumber impurities absorption peaks are due to the surface adsorbed organic precursors during the synthesis or the characterization processes. The effect of these organic impurities is most dominant for nanoparticles due to high surface to volume ratio, whereas these impurity peaks vanish gradually in bulk samples.

The electronic properties of complex oxides provide the interesting fundamental information on chemical bonding, hybridization and the interplay between charge, structure and strain. The room temperature UV–vis absorption spectra of $Bi_{1-x}Ba_xFeO_3$ nanoparticles are shown in the

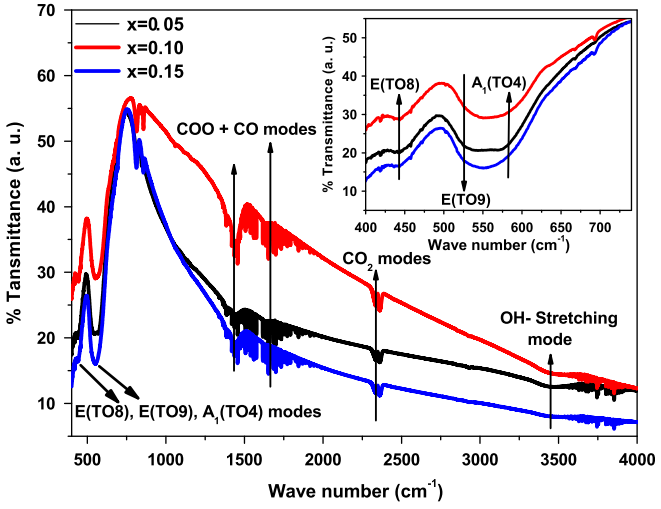

Fig. 5. FTIR transmittance spectra of $Bi_{1-x}Ba_xFeO_3$ nanoparticles. Inset shows the FTIR transmittance spectra in the wavenumber range 400–750 cm^{-1}.

Table 1
Comparison of observed Raman modes for $Bi_{1-x}Ba_xFeO_3$ nanoparticles with reported theoretical Raman data on BFO [22], experimental Raman data on bulk BFO [23] and experimental IR data on nanocrystalline BFO [21]

Modes	$x=0.05$	$x=0.10$	$x=0.15$	Hermet et al. (Theortical)	Porporati et al. (Polycrystalline)	Chen et al. (Nanocrystalline)
E(TO1)	71.5	73	75.2	102	76	77.3
E(TO2)	129.5	133.5	137.8	152	136	133.9
A_1(TO1)	168	169.5	170.2	167	–	150.5
E(TO3)	204.2	212.2	217.1	237	–	226.2
E(TO4)	239.3	258.8	263.5	263	261	–
A_1(TO2)	–	–	–	266	–	–
E(TO5)	271.5	280	300.2	274	281	279.1
A_1(TO3)	322.9	330.4	340.87	318	–	318.7
E(TO6)	356.6	365.4	369.2	335	320	351.8
E(TO7)	–	–	–	378	372	383.5
E(TO8)	438.4	457.8	467.1	409	444	444.1
E(TO9)	535.9	547	549.7	509	530	536.8
A_1(TO4)	616.5	614.3	611.1	517	–	575.5

inset of Fig. 6. The UV–vis absorption spectra show the broad absorbance peak around 475, 490 and 560 nm for $x=0.05$, 0.10 and 0.15 samples, respectively, which are assigned to intrinsic electronic transitions. This broad absorption band is due to the overlapping of electronic transition from $6A_1$ state to $4T_1$ (4G) state and $6A_1$ to 4E, $4A_1$ (4G) ligand field transitions [28]. The optical energy band gap for $Bi_{1-x}Ba_xFeO_3$ nanoparticles was calculated by classical Tauc's relation [29] as given by $\alpha h\upsilon = A(h\upsilon - E_g)^n$, where A is a constant, $h\upsilon$ is the photon energy, E_g is the energy band gap, α is the absorption coefficient. The absorption coefficient is given by $\alpha = (1/d)*\ln(1/T)$, where T is transmittance and d is the thickness of cuvette which is 10 mm in the present case. The value of $n=1/2$, 3/2, 2, or 3 depends on the nature of the electronic transition responsible for the absorption. The value of $n=1/2$ allows for direct transition, thereby giving the direct band gap. The plots of $(\alpha h\upsilon)^2$ versus $h\upsilon$ for $x=0.05$, 0.10 and $x=0.15$ samples are shown in Fig. 6. The extrapolation of the linear region of these plots to $(\alpha h\upsilon)^2=0$ (towards x-axis) gives the corresponding direct energy band gap. The band gap was found to be 2.48, 2.30 and 2.04 eV for $x=0.05$, 0.10 and 0.15 samples respectively. The decrease in band gap may be ascribed to the defect levels introduced between valance band and conduction band with increasing Ba concentration in BFO samples. The observed band gap of $Bi_{1-x}Ba_xFeO_3$ nanoparticles are comparable with the pure BFO nanoparticles, the alkaline earth metal (Ca and Sr) doped and transition metal (Mn and Ni) doped BFO nanoparticles [21,30–33]. The variation in band gap of Ba doped BFO nanoparticles show the incorporation of the Ba ions in BFO lattice.

The magnetic hysteresis (M–H) loops of $Bi_{1-x}Ba_xFeO_3$ nanoparticles with $x=0.05$, 0.10 and 0.15 are shown in Fig. 7. The room temperature saturated M–H loops exhibit the weak ferromagnetic behavior of $Bi_{1-x}Ba_xFeO_3$ nanoparticles. It is known that BFO has G-type antiferromagnetic

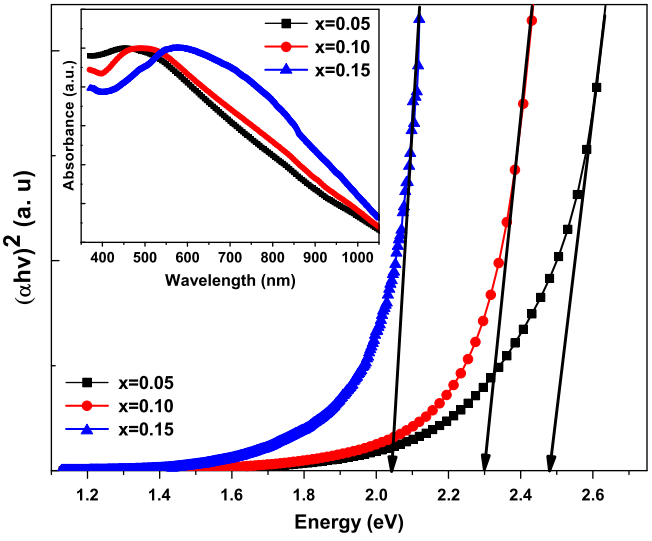

Fig. 6. Plot of $(\alpha h\upsilon)^2$ versus energy for $Bi_{1-x}Ba_xFeO_3$ nanoparticles. Inset shows UV–vis absorbance spectra of $Bi_{1-x}Ba_xFeO_3$ nanoparticles.

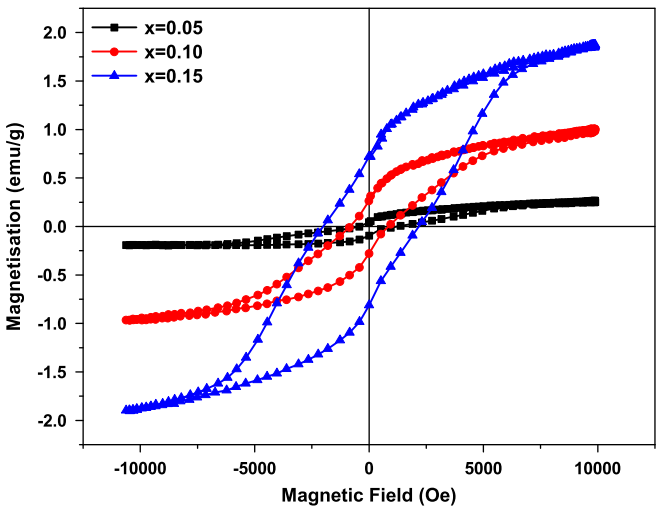

Fig. 7. Magnetization Hysteresis loops for $Bi_{1-x}Ba_xFeO_3$ nanoparticles at room temperature.

ordering superimposed with a spiral spin structure of long period (62 nm). The origin of the weak ferromagnetism is attributed to the nano-size grains in the samples. The uncompensated magnetic moments arising from the antiferromagnetic core and ferromagnetic surface of the nanoparticles might contribute to the weak ferromagnetic behavior of $Bi_{1-x}Ba_xFeO_3$ nanoparticles. With decreasing particle size, surface to volume ratio becomes very large and antiferromagnetic ordering is interrupted at the particle surface and these uncompensated ferromagnetic spins contribute to the net magnetization [34]. The remnant magnetization ($2M_r$) of 0.142, 0.549 and 1.53 emu/g were observed for $x=0.05$, 0.10 and 0.15 samples, respectively. The remnant magnetization and the coercive field increase with increasing Ba concentration in BFO samples. There could be two reasons contributing to the enhancement of ferromagnetism with increasing Ba content in BFO samples. First, the substitution of the Ba^{2+} ions in BFO lattice distorted the rhombohedral structure of BFO resulting in the enhancement of the net magnetization with increasing Ba content in BFO samples. The distorted rhombohedral perovskite structure of BFO allows a weak ferromagnetic ordering due to canting of spins [35–36]. The distortion in rhombohedral structure of BFO caused by the Ba^{2+} substitution suppressed the spiral spin structure released the latent magnetization. Second, the addition of the Ba^{2+} ions for the Bi^{3+} ions in BFO lattice requires charge compensation, which can be achieved by the formation of Fe^{4+} or oxygen vacancies. If Fe^{4+} exists, the statistical distribution of Fe^{3+} and Fe^{4+} ions in octahedral may also lead to the net magnetization and ferromagnetism [37].

The room temperature frequency dependent dielectric constant (ε') and dielectric loss (Tan δ) in the range 100 Hz to 100 kHz for $Bi_{1-x}Ba_xFeO_3$ samples are shown in inset of Fig. 8. It is evident that the dielectric constant (ε') and dielectric loss (Tan δ) decrease with increasing frequency. The increase in the value of ε' at low frequency is due to the presence of various type of polarization factor such as

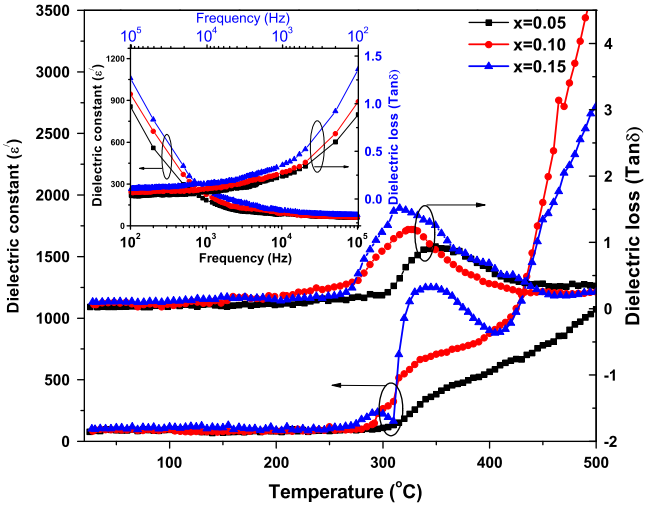

Fig. 8. Temperature dependent plots of ε' and Tan δ for $Bi_{1-x}Ba_xFeO_3$ samples at 100 kHz. Inset shows room temperature frequency dependence of ε' and Tan δ of $Bi_{1-x}Ba_xFeO_3$ samples.

interfacial dislocations, dipolar, ionic, atomic and electronic which becomes significant at low frequencies. The contributions from the core of the nanoparticles will be significant at the higher frequencies and the surface of the nanoparticles and their boundaries with other particles will contribute at relatively low frequencies [38]. It is also observed that the dielectric constant (ε') and dielectric loss (Tan δ) increase with increasing Ba content in BFO samples. The substitution of the Ba^{2+} ions in BFO is expected to introduce more oxygen vacancies due to charge compensation which in turn increases the probability of the hoping conduction mechanism and results in higher value of the dielectric loss. This type of behavior was also observed in the Sr^{2+} and the Pb^{2+} doped BFO ceramics [39,40]. The temperature dependence of ε' and Tan δ at 100 kHz frequency for $Bi_{1-x}Ba_xFeO_3$ samples are shown in Fig. 8. The ε' and Tan δ show anomaly in the vicinity of antiferromagnetic Neel temperature for $Bi_{1-x}Ba_xFeO_3$ samples. The Landau–Devonshire theory of phase transitions predicated this type of dielectric anomaly in magnetoelectrically ordered systems as an effect of vanishing magnetic order on the electric order [5]. The dielectric anomaly due to the coupling between electric and magnetic orders is quite prominent in $x=0.15$ sample in the sense that the change $\Delta\varepsilon'$ in ε' at Neel temperature (T_N) is more as compared to $x=0.10$ and $x=0.05$ samples indicating that incresing Ba doping in BFO increases coupling between electric and magnetic order parameters.

4. Conclusions

In summary, $Bi_{1-x}Ba_xFeO_3$ nanoparticles were synthesized by sol–gel route. Rietveld refinement of the XRD patterns demonstrated the pure phase formation (except $x=0.05$) of $Bi_{1-x}Ba_xFeO_3$ nanoparticles. The distortion created by Ba substitution in BFO lattice was also reflected by Raman and FTIR spectra. The UV–vis measurements showed that the band gap of BFO can be tuned within the visible range by Ba substitution. The magnetic measurements showed the room temperature ferromagnetic behavior and enhancement in the remnant magnetization with increasing Ba doping which is attributed to uncompensated spin moments of the surface of the nanoparticles together with the structural distortion. A noticeable change in the dielectric constant near Neel temperature showed the magnetoelectric coupling between electric and magnetic orders. The room temperature ferromagnetism along with tunable optical band gap in visible region of $Bi_{1-x}Ba_xFeO_3$ nanoparticles may find potential applications in photocatalytic activity and optoelectronic devices.

Acknowledgment

This work was financially supported by Department of Science and Technology (DST) India through Grant no. SR/FTP/PS-91/2009. The authors are thankful to Dr. Pankaj Sharma (JUIT Waknaghat) for helping in UV–vis measurements. The authors are also thankful to INUP program (IISc Bangalore) for Raman measurements.

References

[1] M. Fiebig, Th. Lottermoser, D. Fröhlich, A.V. Goltsev, R.V. Pisarev, Observation of coupled magnetic and electric domains, Nature 419 (2002) 818–820.
[2] N.A. Hill, Why are there so few magnetic ferroelectrics, Journal of Physical Chemistry 104 (2000) 6694–6709.
[3] M. Fiebig, Revival of the magnetoelectric effect, Journal of Physics D 38 (2005) R123–R152.
[4] G.A. Smolenskii, I.E. Chupis, Ferroelectromagnets, Soviet Physics Uspekhi 25 (1982) 475–493.
[5] W. Eerenstein, N.D. Mathur, J.F. Scott, Multiferroic and magnetoelectric materials, Nature 442 (2006) 759–765.
[6] G. Catalan, J.F. Scott, Physics and applications of bismuth ferrite, Advanced Materials 21 (2009) 2463–2485.
[7] V.A. Khomchenko, D.A. Kiselev, J.M. Vieira, Li Jian, A.L. Kholkin, A.M.L. Lopes, Y.G. Pogorelov, J.P. Araujo, M. Maglione, Effect of diamagnetic Ca, Sr, Pb, and Ba substitution on the crystal structure and multiferroic properties of the $BiFeO_3$ perovskite, Journal of Applied Physics 103 (2008) 024105–024110.
[8] M. Arora, P.C. Sati, S. Chauhan, H. Singh, K.L. Yadav, S. Chhoker, M. Kumar, Structural, magnetic and optical properties of $Bi_{1-x}Dy_xFeO_3$ nanoparticles synthesized by sol–gel method, Materials Letters 96 (2013) 71–75.
[9] P.C. Sati, M. Arora, S. Chauhan, S. Chhoker, M. Kumar, Structural, magnetic and optical properties of Pr and Zr codoped $BiFeO_3$ multiferroic ceramics, Journal of Applied Physics 112 (2012) 094102–094107.
[10] Y. Du, Z.X. Cheng, S.X. Dou, M. Shahbazi, X.L. Wang, Enhancement of magnetization and dielectric properties of chromium-doped $BiFeO_3$ with tunable morphologies, Thin Solid Films 518 (2010) e5–e8.
[11] F. Gao, X. Chen, K. Yin, S. Dong, Z. Ren, F. Yuan, T. Yu, Z. Zou, J.M. Liu, Visible-light photocatalytic properties of weak magnetic $BiFeO_3$ nanoparticles, Advanced Materials 19 (2007) 2889–2892.
[12] K. Takahashi, N. Kida, M. Tonouchi, Terahertz radiation by an ultrafast spontaneous polarization modulation of multiferroic $BiFeO_3$ thin films, Physical Review Letters 96 (2006) 117402–117405.

[13] R. Das, K. Mandal, Magnetic, ferroelectric and magnetoelectric properties of Ba-doped $BiFeO_3$, Journal of Magnetism and Magnetic Materials 324 (2012) 1913–1918.
[14] D.H. Wang, W.C. Goh, M. Ning, C.K. Ong, Effect of Ba doping on magnetic, ferroelectric, and magnetoelectric properties in multiferroic $BiFeO_3$ at room temperature, Applied Physics Letters 88 (2006) 212907–212909.
[15] M. Arora, P.C. Sati, S. Chauhan, S. Chhoker, A.K. Panwar, M. Kumar, Structural, optical and multiferroic properties of $BiFeO_3$ nanoparticles synthesized by soft chemical route, Journal of Superconductivity and Novel Magnetism 26 (2013) 443–448.
[16] A. Azam, A. Jawad, A.S. Ahmed, M. Chaman, A.H. Naqvi, Structural, optical and transport properties of Al^{+3} doped $BiFeO_3$ nanopowder synthesized by solution combustion method, Journal of Alloys and Compounds 509 (2011) 2909–2913.
[17] J. Rodriguez-Carvajal, FullProf: A Rietveld Refinement and Pattern Matching Analysis Program (Version: April 2008), Laboratoire Léon Brillouin (CEA-CNRS), France, 2000.
[18] S. Goswami, D. Bhattacharya, P. Choudhury, Particle size dependence of magnetization and noncentrosymmetry in nanoscale $BiFeO_3$, Journal of Applied Physics 109 (2011) 07D737 –07D739.
[19] L.B. McCusker, R.B. Von Dreele, D.E. Cox, D. Louër, P. Scardi, Rietveld refinement guidelines, Journal of Applied Crystallography 32 (1999) 36–50.
[20] G.K. Williamson, W.H. Hall, X-ray line broadening from filed aluminium and wolfram, Acta Metallurgica 1 (1953) 22–31.
[21] P. Chen, X. Xu, C. Koenigsmann, A.C. Santulli, S.S. Wong, J.L. Musfeldt, Size-dependent infrared phonon modes and ferroelectric phase transition in $BiFeO_3$ nanoparticles, Nano Letters 10 (2010) 4526–4532.
[22] P. Hermet, M. Goffinet, J. Kreisel, Ph. Ghosez, Raman and infrared spectra of multiferroic bismuth ferrite from first principles, Physical Review B 75 (2007) 220102–220105.
[23] A.A. Porporati, K. Tsuji, M. Valant, A.K. Axelsson, G. Pezzotti, Raman tensor elements of Multiferroic $BiFeO_3$ with rhombohedral R3C symmetry, Journal of Raman Spectroscopy 41 (2010) 84–87.
[24] M. Ghosh, N. Dilawar, A.K. Bandyopadhyay, A.K. Raychaudhuri, Phonon dynamics of Zn(Mg,Cd)O alloy nanostructures and their phase segregation, Journal of Applied Physics 106 (2009) 084306–084311.
[25] B. Bhushan, Z. Wang, J.V. Tol, N.S. Dalal, A. Basumallick, N.Y. Vasantacharya, S. Kumar, D. Das, Tailoring the magnetic and optical characteristics of nanocrystalline $BiFeO_3$ by Ce doping, Journal of American Ceramic Society 95 (6) (2012) 1985–1992.
[26] K.K. Som, S. Molla, K. Bose, B.K. Chaudhuri, Nonlinear physical properties of amorphous $Bi_4Sr_3Ca_3Cu_yO_x$ semiconducting oxide with y between 0 and 5, Physical Review B 45 (1992) 1655–1659.
[27] B. Sreedhar, C.S. Vani, D.K. Devi, M.V.B. Rao, C. Rambabu, Shape controlled synthesis of barium carbonate microclusters and nanocrystallites using natural polysachharide—gum acacia, American Journal of Materials Science 2 (2012) 5–13.
[28] A. Jaiswal, R. Das, K. Vivekanand, P.M. Abraham, S. Adyanthaya, P. Poddar, Effect of reduced size on the magnetic properties of chemically synthesized $BiFeO_3$ nanocrystals, Journal of Physical Chemistry C 114 (2010) 2108–2115.
[29] J. Tauc, Amorphous and Liquid Semiconductors, Plenum Press, New York, 1974.
[30] B. Bhushan, A. Basumallick, S.K. Bandopadhyay, N.Y. Vasanthacharya, D. Das, Effect of alkaline earth metal doping on thermal, optical, magnetic and dielectric properties of $BiFeO_3$ nanoparticles, Journal of Physics D: Applied Physics 42 (2009) 065004–065011.
[31] X. Yu, X. An, Enhanced magnetic and optical properties of pure and (Mn, Sr) doped $BiFeO_3$ nanocrystals, Solid State Communications 149 (2009) 711–714.
[32] D.K. Mishra, X. Qi, Energy levels and photoluminescence properties of nickel doped bismuth ferrite, Journal of Alloys and Compounds 504 (2010) 27–31.
[33] S. Chauhan, M. Kumar, S. Chhoker, S.C. Katyal, H. Singh, M. Jewariya, K.L. Yadav, Multiferroic, magnetoelectric and optical properties of Mn doped $BiFeO_3$ nanoparticles, Solid State Communications 152 (2012) 525–529.
[34] J.P. Tae, C. Georgia, J.V. Arthur, M.R. Arnold, S.W. Stanislaus, Size-dependent magnetic properties of single-crystalline Multiferroic $BiFeO_3$ nanoparticles, Nano Letters 7 (3) (2007) 766–772.
[35] I. Sosnowska, T. Peterlin-Neumaier, E. Streichele, Spiral magnetic ordering in bismuth ferrite, Journal of Physics C: Solid State Physics 15 (1982) 4835–4846.
[36] Y.F. Popov, A.K. Zvezdin, G.P. Vorob'ev, A.M. Kadomtseva, V.A. Murashev, D.N. Rakov, Linear magnetoelectric effect and phase transitions in bismuth ferrite, $BiFeO_3$, JETP Letters 57 (1993) 69–73.
[37] M.M. Kumar, A. Srinivas, S.V. Suryanarayana, Spontaneous magnetic moment in $BiFeO_3$–$BaTiO_3$ solid solutions at low temperatures, Journal of Magnetism and Magnetic Materials 188 (1998) 203–212.
[38] U. Inatatha, S. Eitssayeam, J. Wang, T. Tunkasiri, Impedance study of the dielectric permittivity in $BaFe_{0.5}Nb_{0.5}O_3$ perovskite ceramic, Current Applied Physics 10 (2010) 21–25.
[39] A. Reetu, S. Agarwal, Sanghi, N. Ashima, Monica Ahlawat, Phase transformation, dielectric and magnetic properties of Nb doped $Bi_{0.8}Sr_{0.2}FeO_3$ multiferroics, Journal of Applied Physics 111 (2012) 113917–113923.
[40] R. Mazumder, A. Sen, Effect of Pb-doping on dielectric properties of $BiFeO_3$ ceramics, Journal of Alloys and Compounds 475 (2009) 577–580.